JGR Solid Earth

RESEARCH ARTICLE
10.1029/2023JB027725

On the Constitutive Equations for Coupled Flow, Chemical Reaction, and Deformation of Porous Media

Viktoriya M. Yarushina[1], **Yury Y. Podladchikov**[2], **and Hongliang Wang**[1]

[1]Institute for Energy Technology, Kjeller, Norway, [2]University of Lausanne, Lausanne, Switzerland

Key Points:

- A new model for porosity and solid volume change during coupled hydro-mechano-chemical processes is proposed
- Model predicts the dependence of elastic and viscous properties on reaction progress and fluid composition
- Model explains the possibility of achieving a complete reaction and preservation of porosity during chemical reactions

Correspondence to:
V. M. Yarushina,
viktoriya.yarushina@ife.no

Citation:
Yarushina, V. M., Podladchikov, Y. Y., & Wang, H. (2023). On the constitutive equations for coupled flow, chemical reaction, and deformation of porous media. *Journal of Geophysical Research: Solid Earth*, *128*, e2023JB027725. https://doi.org/10.1029/2023JB027725

Received 24 AUG 2023
Accepted 5 DEC 2023

Author Contributions:
Conceptualization: Viktoriya M. Yarushina, Yury Y. Podladchikov
Formal analysis: Viktoriya M. Yarushina
Funding acquisition: Viktoriya M. Yarushina
Investigation: Viktoriya M. Yarushina
Methodology: Viktoriya M. Yarushina, Yury Y. Podladchikov
Project Administration: Viktoriya M. Yarushina
Resources: Viktoriya M. Yarushina
Software: Viktoriya M. Yarushina, Hongliang Wang
Supervision: Viktoriya M. Yarushina
Validation: Viktoriya M. Yarushina, Hongliang Wang
Visualization: Viktoriya M. Yarushina
Writing – original draft: Viktoriya M. Yarushina

Abstract Deformation, chemical reactions, fluid flow in geological formations, and many engineering materials are coupled processes. Most existing models of chemical reactions coupled with fluid transport assume the dissolution-precipitation process or mineral growth in rocks. However, these models have limitations, such as predicting restricted reaction extent due to pore clogging or disregarding porosity changes resulting from mineral growth. Recent studies indicate mineral replacement involves coupled dissolution-precipitation, maintaining porosity while altering the solid volume. This has multiple practical implications for natural geological processes and within petroleum and environmental engineering. We present a novel model for reaction-driven mineral expansion that preserves porosity and allows solid volume change. First, we look at fluid-rock interaction at the pore scale and derive effective rheology of a reacting porous media. On a larger scale, we adopt a two-phase continuum medium approach to investigate the coupling between reaction, deformation, and fluid flow. Our micromechanical model based on observations assumes that rock or cement consists of an assembly of solid reactive grains, initially composed of a single, pure phase. The reaction occurs at the fluid-solid contact and progresses into the solid grain material. We approximate the pores and surrounding solid material as an idealized cylindrical shell to simplify the problem and obtain tractable results. We derive macroscopic stress-strain constitute laws that account for chemical alteration and viscoelastic deformation of porous rocks. Our model explains the possibility of achieving a complete reaction, preservation of porosity during chemical reactions, and dependence of mechanical rock properties on fluid chemistry.

Plain Language Summary Reducing global greenhouse gas emissions depends upon developing carbon capture and storage (CCS) technology that injects CO_2, a main greenhouse gas, into geological formations. Mafic and ultramafic rocks can absorb CO_2 and thus provide leak-proof permanent CO_2 removal from the atmosphere. However, there are still questions about whether this process can happen quickly enough to be practical. CO_2 injection involves cement-secured wells, but CO_2 impurities may compromise cement quality through carbonation. Reliable models are vital for designing storage sites, yet predicting chemical reactions' effects on flow and deformation remains challenging. Our innovative approach employs recent experimental data to develop a new model. By examining fluid-rock interactions on a small scale, we extrapolate to larger behaviors. Notably, rocks and cement can react with fluids, retaining porosity post-alteration. This insight should be integrated into prevailing models. The model also indicates possible expansion during reactions, potentially affecting structures or aiding in well decommissioning to prevent leakage. In summary, CCS hinges on addressing the complexities of the subsurface's geological uncertainty and CO_2 behavior. Our new model informs injectivity, storage capacity, and potential hazards contributing to sustainable practices.

1. Introduction

CO_2 storage in geological formations is one of the elements of the global solution for reducing greenhouse gas emissions. Several pilot CO_2 injection projects have been established all over the world. Based on its long-standing experience with subsurface operations, the petroleum industry chose deep saline aquifers or depleted oil and gas reservoirs for CO_2 injection. These are widely available and have good storage capacity (Boait et al., 2012; Elenius et al., 2018; Riis & Halland, 2014). The major leakage risk is associated with wellbore integrity, which might be compromised due to cement deterioration during exposure to CO_2 and aggressive impurities that might be present in the CO_2 stream. Thus, much work has been focused on improving cement compositions (Vralstad et al., 2019; Wolterbeek et al., 2018; Zhang & Bachu, 2011). On the other hand, Academia has been favoring CO_2 storage in mafic and ultramafic rocks, arguing that carbon mineralization occurring at CO_2 contact with these rocks is the best way to secure permanent CO_2 storage. However, for many years, there has been a debate on whether a

complete reaction to CO_2 can be achieved in a reasonable timeframe. Early laboratory estimates of the reaction rate predicted mineralization would take thousands of years (Kelemen & Matter, 2008). Proponents of mineral carbon capture and storage (CCS) argued that the force of crystallization brought by the reaction might cause fracturing and enhance the reaction's progress (Kelemen & Hirth, 2012; Yarushina & Bercovici, 2013). Another related question was how rocks could undergo 100% hydration/carbonation. While early models predicted that fluid-rock reactions involving an increase in solid volume are self-limiting (Aharonov et al., 1998), field observations showed 100% hydrated peridotites (serpentinites) and carbonated peridotites (listvenites) (Kelemen & Matter, 2008). This discussion continued until the first pilot study on CO_2 injection in basalts was established in Iceland. The results showed that 95% of injected CO_2 was mineralized in fractured and unfractured basalts after 2 years of injection (Clark et al., 2020; Matter et al., 2016). This revealed an obvious gap between theoretical understanding and practice. The Paris Agreement requires accelerating CCS and establishing even more CO_2 injection sites in sandstones, basalts, and carbonates while decreasing costs. This ultimately requires injecting increased quantities of CO_2 without separating it from highly reactive common impurities such as H_2S. CO_2 and H_2S react with the basaltic rocks, liberating divalent cations, Ca^{2+}, Mg^{2+}, and Fe^{2+}, precipitating stable carbonate and sulfide minerals. In nature, the same processes are associated with serpentinization and surface weathering in ultramafic and mafic rocks exposed to water. In cement and basalts, H_2S reacts with lime (CaO) and ferrite to produce calcium sulfide (CaS) and pyrite (Hu et al., 2006; Kutchko et al., 2011; Matter et al., 2016).

Deformation, chemical reactions, and fluid flow in geological formations and wellbore cement are coupled processes. Most existing models of chemical reactions coupled with fluid transport either assume the dissolution-precipitation process (Rutter, 1976; Weyl, 1959) or mineral growth in rocks (Fletcher & Merino, 2001; Schmid et al., 2009; Steiger, 2005). However, dissolution-precipitation models predict a very limited extent of reaction hampered by pore clogging and blocking reactive surfaces, which will stop reaction progress due to limited fluid supply to reactive surfaces. This contradicts field observations reporting that natural rocks can undergo 100% hydration/carbonation (Evans et al., 2018). Mineral growth models, on the other hand, preserve solid volume but do not consider its feedback on porosity evolution (Fletcher & Merino, 2001).

Merino and Dewers (1998) describe mineral replacement in rocks as the growth of guest minerals and dissolution of the host associated with the generation of stress at the grain contacts. However, they assume volume conservation during the reaction. Putnis et al. (2021), who studied a range of reactions, including carbonate minerals growth and cement degradation using nanoscale imaging of mineral surfaces during crystallization, also define mineral replacement as a coupled dissolution-precipitation process. They indicate that porosity is preserved, allowing fluid to maintain contact with a reaction interface, and they question the classical crystal growth theories. Malvoisin et al. (2021) made observations of a serpentine vein in serpentinized dunite collected at depth during the Oman Drilling Project. They suggested that mineral replacement reactions such as serpentinization increase the solid volume as in dissolution-precipitation models and preserve porosity as in mineral growth models. The deformation of the solid volume rather than porosity clogging accommodates the observed increase in solid volume. They also found that aqueous species transport is limited, and reaction products do not precipitate in the pores but stay attached to the primary mineral.

Chemical reactions associated with volume increase have multiple practical implications. They might be hazardous. For example, the crystallization of sodium sulfate salts in confined pores is the main cause of damage to building materials and a loss of cultural heritage (Marzal & Scherer, 2008). The durability of concrete may be compromised due to an external sulfate attack, characterized by the ingress of sulfate ions from the surrounding medium, finally leading to the expansion of solid volume, cracking, spalling, and eventually to the complete disintegration of the material (Idiart et al., 2011). It is generally accepted that the cause of these expansions is the formation of ettringite from the sulfate ions and the different aluminate phases in the hardened cement paste. Swelling or shrinkage of smectite when exposed to water or supercritical CO_2 may also lead to the formation of microcracks (e.g., Schaef et al., 2012; L. L. Wang et al., 2014). This implies that the exposure of clay-rich caprocks to CO_2 and the resulting dehydration and shrinkage may lead to increased caprock permeability and CO_2 leakage, at least along the injection wellbore (Busch et al., 2016). On the other hand, chemical reactions associated with solid volume increase might be useful. Reaction-driven mineral expansion associated with hydration of some solid additives, such as quicklime and periclase, may be utilized in plugging and abandonment of old petroleum wells to prevent leakage between plug and caprock or between plug and casing (Ostapenko, 1976; Wolterbeek et al., 2018). In a geological context, mineral expansion and shrinkage are important in pseudomorphic

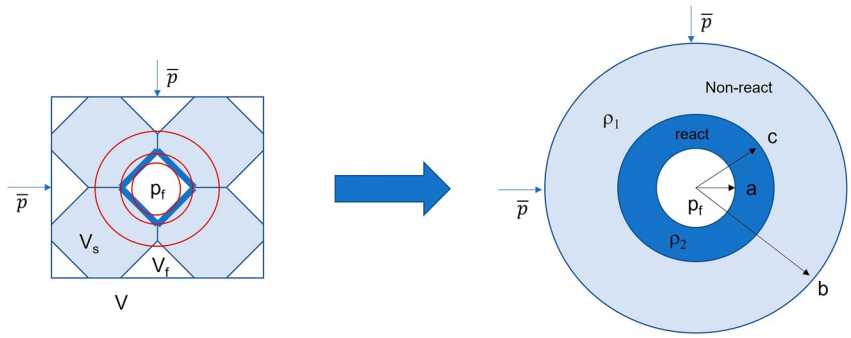

Figure 1. Schematic model for porosity preserving mineral replacement reaction. (a) The total volume, V, consists of solid grains, V_s, in contact with each other and pore fluid, V_f. The reaction starts at the fluid-solid contact and progresses into the solid volume (dark blue). The fluid pressure, p_f, and the external total pressure, p_t, act on the volume in a viscous model. In the elastic model, the rates of fluid pressure, $\dot{p}_f$, and total pressure, $\dot{p}_t$, are prescribed at the internal and external boundaries of the volume, respectively. (b) Representative Volume Element (RVE) for mineral replacement reaction in porous media. The reaction starts around the cylindrical pore and progresses into the initial solid phase, preserving porosity. Reacted and non-reacted materials have different densities and mechanical properties. Pore radius, a, and radius of RVE, b, are determined by porosity. A reaction rim of radius c grows into the shell starting from the pore radius, a.

replacement and vein formation (Fletcher & Merino, 2001; Malvoisin et al., 2021; Merino & Dewers, 1998; Perchuk et al., 2023).

Here, we propose a new model for porosity-preserving reaction-driven mineral expansion. Models based on poromechanics are needed to fully account for the coupling between reaction, deformation, and fluid flow. We derive macroscopic poroviscoelastic stress-strain constitute laws that account for chemical alteration and viscoelastic deformation of porous rocks. These constitutive equations can be used in reactive transport models. We investigate the role of deformation parameters and reaction rate on the fluid flow and the possibility of achieving a complete reaction. Our model explains several experimental observations, including changes in mechanical properties during the reaction.

2. Effective Rheology of Reacting Porous Media

Let's consider a porous matrix fully saturated with a single reactive fluid. First, we look at fluid-rock interaction at the pore scale and derive effective rheology of a reacting porous media. On a larger scale, we use a two-phase continuum medium approach to investigate the coupling between reaction, deformation, and fluid flow. Our micromechanical model is based on observations from Malvoisin et al. (2020) and Putnis et al. (2021) that the transport of dissolved species is restricted to a scale below the grain size. We assume that rock or cement consists of an assembly of solid reactive grains, initially composed of a single, pure phase (Figure 1a). The reaction occurs at the fluid-solid contact and progresses into the solid grain material. The pore space is fully saturated with a reacting fluid, which is assumed to be well mixed and have a homogeneous fluid pressure, p_f, that might change in time due to, for example, precipitation on the inner surface or fast dehydration reactions (see Table 1 for notations). Before any reaction, the initial solid phase is assumed to be under homogeneous hydrostatic stress, p_t. In addition, we assume that the reaction occurs under isothermal conditions. We assume that volume change during the reaction is accommodated by deformation. Various geomaterials, including basaltic rocks and cement, exhibit instantaneous elastic deformation and time-dependent creep (Heap et al., 2011; Minde & Hiorth, 2020; Neville et al., 1983; Sabitova et al., 2021; Wolterbeek et al., 2016; Yarushina et al., 2021). Thus, in our model, we consider these two different end-member behaviors. To simplify the problem and obtain tractable results, we approximate the pores and surrounding solid material as an idealized cylindrical shell (Figure 1b). Previous studies show that pore geometry has little effect on the form of resulting constitutive laws for porous materials but affects the expressions for effective moduli (Yarushina & Podladchikov, 2015; Zimmerman, 1991).

As the reaction begins, the mechanical equilibrium in the solid phase will be disturbed, but due to cylindrical symmetry, it will depend only on the radial coordinate, r. Macroscopic porosity, which is a fluid volume fraction, determines the pore radius, a, and the outer radius of a cylindrical shell, b, so that

$$\varphi = V_f / V = a(t)^2 / b(t)^2 \quad (1)$$

Table 1
List of Principal Notations

Symbol	Meaning	Unit
a	Internal radius of RVE	m
b	The external radius of RVE	m
B	Skempton's coefficient	
c	Position of the reaction front in RVE	m
Da	Dahmköhler number	
De	Deborah number	
g_j	Gravity	m/s^2
G	Elastic shear modulus	Pa
k	Permeability	m^2
K	Elastic bulk modulus	Pa
L	Domain length	m
n	Permeability exponent	
$\bar{p}$, p_f, p_e	Total, fluid, and effective pressure	Pa
q_D	Darcy's flux	m/s
r	Radial coordinate within RVE	m
t	Time	s
v	Velocity within RVE	m/s
v_s,v_f	Solid and fluid velocity	m/s
V,V_s,V_f	Total, solid, and fluid volumes within RVE	m^2
X_s, X_{seq}	Mass fraction of fluid bound to the solid, equilibrium value	
X_1, X_2	Mass fraction of immobile solid within RVE before and after reaction	
α	Biot-Willis parameter	
ε	Macroscopic volumetric strain	
η	Viscosity	Pa s
Θ	The density ratio of an immobile component before and after the reaction, Equation 9	
κ	Effective compressibility due to reaction	
μ_f	Viscosity of fluid	Pa s
μ_1, μ_2	Solid shear viscosity within RVE	Pa s
ξ	Reaction progress	
ρ	Densities	
σ_i	Components of stress tensor within RVE	Pa
τ_{ij}	Macroscopic tensor of stress deviator	Pa
ϕ	Porosity	

Reaction progress determines the position of a reaction front, c. We define the extent of reaction, $\xi(t)$, as the volume fraction of reacted part of the solid volume:

$$\xi(t) = \frac{c(t)^2 - a(t)^2}{b(t)^2 - a(t)^2} \tag{2}$$

This quantity is closely related to the composition. The reaction kinetics determines its changes and can be modeled using, for example, first-order kinetic law, depending on the reaction. We determine the stress by assuming that the initial non-reacted and reacted phases are isotropic and homogeneous solids characterized by their densities and mechanical properties (Figure 1b).

Two equations are needed to describe the expansion or compaction of porous materials. One describes changes in porosity and the other volumetric deformation of the entire volume. It is practical to rewrite the porosity Equation 1 in the following differential form used in further derivations.

$$\frac{d\varphi}{dt} = \frac{2\varphi}{a}\frac{da}{dt} - \frac{2\varphi}{b}\frac{db}{dt} = 2\varphi\left(\frac{v}{r}\Big|_{r=a} - \frac{v}{r}\Big|_{r=b}\right) \tag{3}$$

where v is the radial velocity of the given Representative Volume Element (RVE). Macroscopic volumetric deformation, ε, is determined by changes in the total volume of RVE

$$\frac{d\varepsilon}{dt} = \frac{1}{V}\frac{dV}{dt} = 2\frac{v}{r}\Big|_{r=b} \tag{4}$$

2.1. Elastic (Viscous) Adjustment of the Matrix

The total compressibility of porous rock is the sum of the compressibility of the pore space and that of the solid mineral grains. Given that the compressibility of mineral grains is roughly two orders of magnitude lower than the compressibility of the pore space (e.g., Yarushina et al., 2013), we omit it from subsequent derivations. Note that even though the solid mineral grains are assumed to be incompressible, the total volume of an RVE changes due to changes in pore volume and deformation around the pore. The addition of the compressibility of solid mineral grains will maintain the same structure of the resulting compaction equations but will lead to more cumbersome relations for effective moduli (Yarushina & Podladchikov, 2015).

The constitutive equations for incompressible linear elastic material relate radial velocity, v, with radial, $\dot{\sigma}_r$, and tangential, $\dot{\sigma}_\theta$, components of stress rates:

$$\frac{v}{r} = \frac{\dot{\sigma}_\theta - \dot{\sigma}_r}{4G} \tag{5}$$

where G is the elastic shear modulus, and the dot represents the material time derivative. Both reacted and non-reacted parts of the solid volume must be in mechanical equilibrium and satisfy the force balance equation and incompressibility condition

$$\frac{\partial \sigma_r}{\partial r} + \frac{\sigma_r - \sigma_\theta}{r} = 0 \tag{6}$$

$$\frac{\partial v}{\partial r} + \frac{v}{r} = 0 \tag{7}$$

Conservation of momentum requires that normal stress be continuous at the reaction front. We assume that the mass of the immobile solid component is conserved, which means that it does not go into the fluid during the reaction. For example, CO_2 and H_2O, chemically bound to the solid, break down and go into the fluid and are therefore not immobile. On the contrary, Mg or Ca has negligible solubility in the fluid and can be considered immobile. Then, for immobile components of the solid, one can write the following jump condition:

$$\rho_1 X_1 v_1 - \rho_2 X_2 v_2\Big|_{r=c} = \frac{dc}{dt}(\rho_1 X_1 - \rho_2 X_2) \tag{8}$$

where X is the mass fraction of the immobile component; index 1 denotes density and velocity in the non-reacted phase, and index 2 marks density and velocity in the reacted phase, respectively. The general definition of the density ratio can be defined as follows:

$$\Theta = \rho_2 X_2 / \rho_1 X_1 \tag{9}$$

Solving Equations 5–8 for each phase, assuming that the rates of fluid and total pressures are prescribed at the internal and external boundaries of the volume, we obtain the following velocities:

$$v_1 = -\frac{1}{r\hat{G}}\left(\Theta\frac{dp_e}{dt} - G_2\frac{\xi\left(b^2 - a^2\right)^2(1-\Theta)}{a^2(a^2 + (b^2 - a^2)\xi)}\frac{d\xi}{dt}\right) \tag{10}$$

Table 2
Coefficients in the Compaction Equations

Elastic	Viscous
$\kappa_\varphi^e = \frac{\varphi(1-\Theta)(1-\varphi)\left(G_1(1-\xi)+G_2\xi\right)}{\Theta G_1(1-\xi)\varphi+G_2\xi}$	$\kappa_\varphi^v = \frac{\varphi(1-\Theta)(1-\varphi)\left(\mu_1(1-\xi)+\mu_2\xi\right)}{\Theta\mu_1(1-\xi)\varphi+\mu_2\xi}$
$\kappa_d^e = \kappa_\varphi^e \frac{G_2\xi}{\varphi\left(G_1(1-\xi)+G_2\xi\right)}$	$\kappa_d^v = \kappa_\varphi^v \frac{\mu_2\xi}{\varphi\left(\mu_1(1-\xi)+\mu_2\xi\right)}$
$\frac{1}{K_\varphi} = \frac{\varphi(1-\Theta\varphi)(\xi+(1-\xi)\varphi)}{(1-\varphi)\left(\Theta G_1(1-\xi)\varphi+G_2\xi\right)}$	$\frac{1}{\eta_\varphi} = \frac{\varphi(1-\Theta\varphi)(\xi+(1-\xi)\varphi)}{(1-\varphi)\left(\Theta\mu_1(1-\xi)\varphi+\mu_2\xi\right)}$
$K_d = K_\varphi\left(\frac{1}{\Theta}-\varphi\right)$	$\eta_d = \eta_\varphi\left(\frac{1}{\Theta}-\varphi\right)$

$$v_2 = -\frac{1}{r\hat{G}}\left(\frac{dp_e}{dt} + G_1\frac{\left(b^2-a^2\right)^2(1-\Theta)(1-\xi)}{b^2(a^2+(b^2-a^2)\xi)}\frac{d\xi}{dt}\right) \tag{11}$$

and stresses around the pore

$$\dot{\sigma}_r^1 = -\frac{dp_t}{dt} + 2\frac{G_1}{\hat{G}}\frac{b^2-r^2}{b^2r^2}\left(\Theta\frac{dp_e}{dt} - G_2\frac{(1-\Theta)\left(b^2-a^2\right)^2\xi}{a^2(a^2+(b^2-a^2)\xi)}\frac{d\xi}{dt}\right) \tag{12}$$

$$\dot{\sigma}_\theta^1 = -\frac{dp_t}{dt} - 2\frac{G_1}{\hat{G}}\frac{b^2+r^2}{b^2r^2}\left(\Theta\frac{dp_e}{dt} - G_2\frac{(1-\Theta)\left(b^2-a^2\right)^2\xi}{a^2(a^2+(b^2-a^2)\xi)}\frac{d\xi}{dt}\right) \tag{13}$$

$$\dot{\sigma}_r^2 = -\frac{dp_f}{dt} - 2\frac{G_2}{\hat{G}}\frac{r^2-a^2}{a^2r^2}\left(\frac{dp_e}{dt} + G_1(1-\Theta)\frac{\left(b^2-a^2\right)^2(1-\xi)}{(a^2+(b^2-a^2)\xi)b^2}\frac{d\xi}{dt}\right) \tag{14}$$

$$\dot{\sigma}_\theta^2 = -\frac{dp_f}{dt} - 2\frac{G_2}{\hat{G}}\frac{a^2+r^2}{a^2r^2}\left(\frac{dp_e}{dt} + G_1(1-\Theta)\frac{\left(b^2-a^2\right)^2(1-\xi)}{(a^2+(b^2-a^2)\xi)b^2}\frac{d\xi}{dt}\right) \tag{15}$$

where $p_e = p_t - p_f$, and

$$\frac{1}{\hat{G}} = \frac{a^2b^2\left(\xi\left(b^2-a^2\right)+a^2\right)}{2(b^2-a^2)(G_1\Theta a^2(1-\xi)+G_2\xi b^2)} \tag{16}$$

Substituting obtained velocities into Equations 3 and 4 we arrive at the following elastic compaction equations for reacting materials:

$$\frac{d\varphi^e}{dt} = -\frac{1}{K_\varphi}\frac{dp_e}{dt} - \kappa_\varphi^e\frac{d\xi}{dt} \tag{17}$$

$$\frac{d\varepsilon^e}{dt} = -\frac{1}{K_d}\frac{dp_e}{dt} + \kappa_d^e\frac{d\xi}{dt} \tag{18}$$

Compressive strains are assumed to be negative here. Effective coefficients in the above equations are defined in Table 2. Depending on the density change, coefficients κ_φ^e and κ_d^e can be either positive or negative. In the limiting case of no reaction (ξ = const), these equations reduce to purely elastic compaction equations derived in Yarushina and Podladchikov (2015) and which are shown to be consistent with Biot's theory of poroelasticity (Biot, 1941) and Gassmann's relations (Gassmann, 1951). The effect of chemical reactions on the porous material is two-fold. They contribute to porosity changes in Equation 17 and to overall volume change Equation 18. Which of these processes dominates depends on the relative importance of the reaction terms in Equations 17 and 18.

Similar analysis can be repeated for viscous rocks, resulting in

$$\frac{d\varphi^v}{dt} = -\frac{p_e}{\eta_\varphi} - \kappa_\varphi^v\frac{d\xi}{dt} \tag{19}$$

$$\frac{d\varepsilon^v}{dt} = -\frac{p_e}{\eta_d} + \kappa_d^v\frac{d\xi}{dt} \tag{20}$$

Coefficients in these equations are defined in Table 2.

2.2. Resulting Constitutive Laws

A macroscopic Maxwell-type viscoelastic model for reaction-induced volume change might be obtained by summing up elastic and viscous contributions to porosity and total volume evolution, namely

$$\frac{d^s\varepsilon}{dt} = -\frac{1}{K_d}\left(\frac{d^sp_t}{dt} - \frac{d^fp_f}{dt}\right) - \frac{p_e}{\eta_d} + \kappa_d\frac{d^s\xi}{dt} \tag{21}$$

$$\frac{d^s\varphi}{dt} = -\frac{1}{K_\varphi}\left(\frac{d^s p_t}{dt} - \frac{d^f p_f}{dt}\right) - \frac{p_e}{\eta_\varphi} - \kappa_\varphi \frac{d^s\xi}{dt} \tag{22}$$

Here, $\frac{d^s}{dt}$ and $\frac{d^f}{dt}$ are the material time derivatives of the solid and fluid phases defined as $\frac{d^s}{dt} = \frac{\partial}{\partial t} + v_s^j \nabla_j$ and $\frac{d^f}{dt} = \frac{\partial}{\partial t} + v_f^j \nabla_j$, respectively. In Equations 21 and 22, the reaction contributes to both porosity changes, as in classical dissolution-precipitation models, and solid volume change, as suggested by Malvoisin et al. (2021). The first two terms give a purely mechanical contribution to compaction, while the last term gives the effect of a chemical reaction. In addition to explicit reactive terms in compaction equations, reactions also affect effective compressibility K_d, K_φ and viscosity η_d, η_φ.

2.3. Properties of a New Model

2.3.1. The Relative Importance of Reactive Terms

Whether volume expansion or porosity clogging will dominate depends on the relative importance of the reactive terms in Equations 21 and 22, that is, on the ratio of effective compressibilities due to the reaction

$$\frac{\kappa_d^e}{\kappa_\varphi^e} = \frac{G_2\xi}{(G_1(1-\xi)+G_2\xi)\varphi}, \frac{\kappa_d^v}{\kappa_\varphi^v} = \frac{\mu_2\xi}{(\mu_1(1-\xi)+\mu_2\xi)\varphi} \tag{23}$$

At the beginning of the reaction when $\xi \ll 1$, the reaction will produce negligible volume expansion and will cause mainly reduction of porosity as in dissolution/precipitation models. As the reaction progresses, the importance of volume expansion becomes comparable to porosity reduction. In low porosity materials or as porosity gets clogged due to reaction, volume expansion becomes more important than porosity clogging, allowing further accommodation of reaction.

2.3.2. Dependence of Elastic and Viscous Properties on Reaction Progress/Fluid Composition

Our model shows that elastic and viscous parameters in reacting rocks depend on reaction progress. Bulk modulus rapidly drops as porosity increases, as often predicted by elastic effective media models (Yarushina & Podladchikov, 2015; Zimmerman et al., 1986). The ongoing chemical reaction can either strengthen the material or soften it, depending on the reaction and elastic properties of the product (Figure 2). For instance, the carbonation of cement that is associated with the conversion of portlandite ($Ca(OH)_2$, $K = 26$ GPa, $\rho = 2.23$ g/cm^3) to denser and harder mineral calcite ($CaCO_3$, $K = 129$ GPa, $\rho = 2.71$ g/cm^3) will lead to a strengthening of cement. Indeed, experiments on the carbonation of Portland cement with wet supercritical CO_2 showed that the elastic moduli of carbonated samples are significantly higher than those of noncarbonated samples (Fabbri et al., 2009). On the other hand, exposure of cement to H_2S will lead to its softening. In this case, H_2S reacts with lime (CaO, $K = 104$ GPa, $\rho = 3.34$ g/cm^3) and ferrite (Fe, $K = 178$ GPa, $\rho = 7.87$ g/cm^3) to produce softer minerals with a smaller density, such as calcium sulfide (CaS, $K = 56$ GPa, $\rho = 2.59$ g/cm^3) and pyrite (FeS_2, $K = 150$ GPa, $\rho = 5$ g/cm^3) (Hu et al., 2006; Kutchko et al., 2011). Thus, whether the development will occur in the softening or strengthening behavior depends on the mechanical properties of minerals constituting pristine and reacted material. More porous materials are easier to deform, that is, their bulk modulus is smaller than that of low-porosity counterparts.

Effective bulk viscosity's dependence on porosity is very similar to non-reactive rocks (Schmeling et al., 2012; Yarushina & Podladchikov, 2015). Like the bulk modulus, effective viscosity might increase or decrease with reaction progress, depending on the properties of the reaction product. In our model, the creep rate linearly depends on the stress (Figure 3). In addition, the creep rate depends on the extent of the reaction and reaction rate, which depends on the chemistry of the reactive fluid. These conclusions align with the observations of Xing et al. (2022), who performed experiments on basalts from the CarbFix site in Iceland. They used both dry samples and samples saturated with different fluids, including pure water and a mixture of water and CO_2. They showed that the creep rate changed with fluid type. Moreover, the creep rate exhibited a linear dependence on the stress (Figure 3).

3. Governing Equations for Coupled Reactions, Deformation, and Flow

Chemical reactions, rock deformation, and fluid flow can be modeled using a two-phase continuum media approach (Malvoisin et al., 2017; Omlin et al., 2017; Yarushina & Podladchikov, 2015). The system of governing equations includes the conservation of total mass

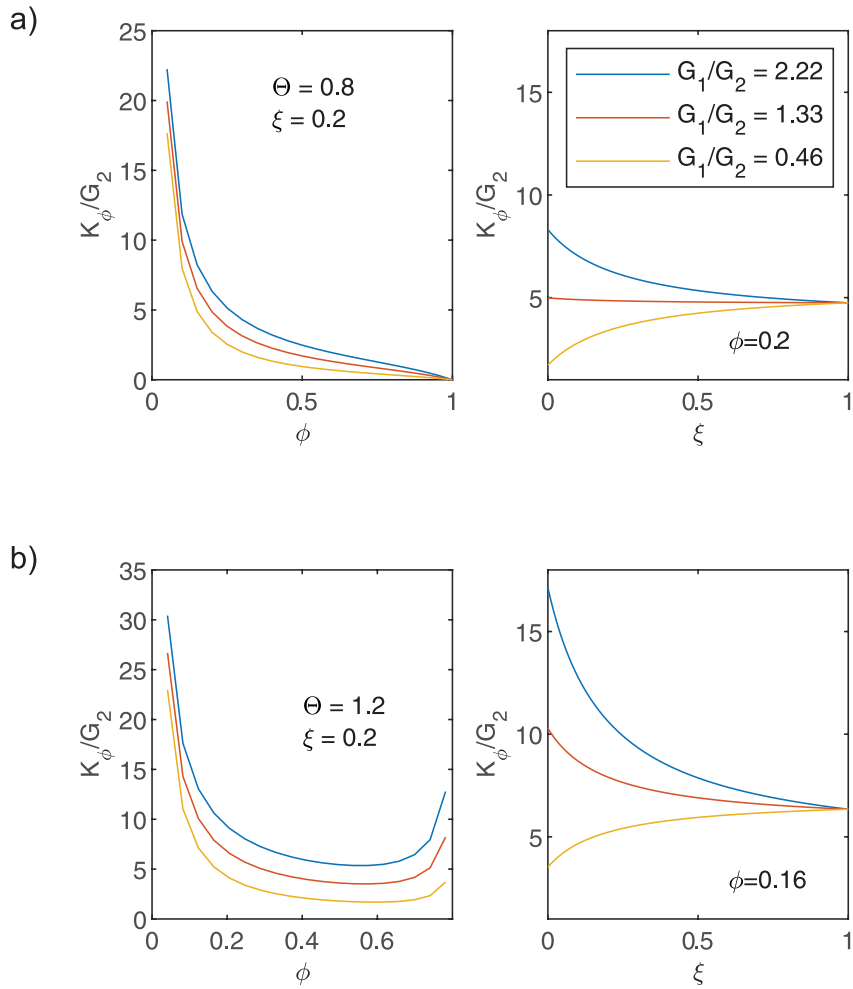

Figure 2. Model predictions for effective bulk modulus in reactive elastic materials. The figure shows dependence on porosity and reaction progress for cases when the original material is denser (a), or the reaction product is denser (b).

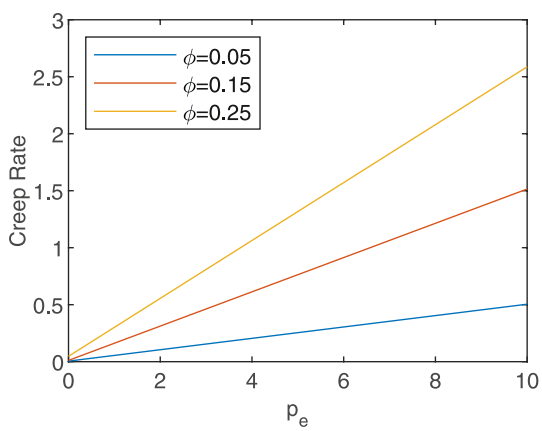

Figure 3. Creep rate versus pressure in reactive materials at different porosities ($\mu_2/\mu_1 = 2$, $\Theta = 0.8$).

$$\frac{\partial(\rho_f\varphi + \rho_s(1-\varphi))}{\partial t} + \nabla_j\left(\rho_f\varphi v_f^j + \rho_s(1-\varphi)v_s^j\right) = 0, \tag{24}$$

conservation of the dry solid mass

$$\frac{\partial(\rho_s(1-X_s)(1-\varphi))}{\partial t} + \nabla_j\left(\rho_s(1-X_s)(1-\varphi)v_s^j\right) = 0, \tag{25}$$

conservation of total momentum

$$\nabla_j(\tau_{ij} - p_t\delta_{ij}) - g_j\rho_t = 0 \tag{26}$$

and Darcy's law

$$\varphi\left(v_f^j - v_s^j\right) = -\frac{k(\varphi)}{\mu_f}(\nabla_j p_f + g_j\rho_f). \tag{27}$$

Here, ρ_s and ρ_f are densities of the solid and fluid phases, $\rho_t = \rho_f\varphi + \rho_s(1-\varphi)$ is the total density, v_s^j and v_f^j are solid and fluid velocity, τ_{ij} is the total deviatoric stress, $k(\varphi)$ is the porosity-dependent permeability, μ_f is the fluid shear viscosity. X_s is the mass fraction of fluid bound to the solid. It is related to the extent of reaction so that $\xi = X_s/X_{\text{seq}}$, where X_{seq} is the mass fraction of fluid

bound in the solid at the equilibrium. The first-order kinetic law for a chemical reaction can be used to model change in composition:

$$\frac{d^s X_s}{dt} = \left(\frac{\varphi}{\varphi_p}\right)^{2/3} \frac{X_{\text{seq}} - X_s}{\tau}, \tag{28}$$

where τ is the characteristic time for reaction and φ_p is the minimum porosity for which a porous rock has the same reactive surface area as a powder. The evolution of reactive surface area during the reaction is modeled as a function of porosity, employing the geometric relationship from Kieffer et al. (1999) and Lichtner (1988). To close this system of equations, we add a fluid equation of state

$$\frac{K_f}{\rho_f}\frac{d^f \rho_f}{dt} = \frac{d^f p_f}{dt}, \tag{29}$$

Carman-Kozeny permeability law:

$$k = k_0(\varphi/\varphi_0)^n \tag{30}$$

and newly derived compaction Equations 21 and 22. Here, K_f is the fluid bulk modulus, k_0 is the reference permeability at φ_0.

We will rewrite mass conservation equations in an alternative form to compare with previous two-phase models without reaction. By introducing the material time derivatives and using Equations 21 and 22 in Equation 25, we obtain the following:

$$\frac{1}{\rho_s}\frac{d^s \rho_s}{dt} = \frac{1}{(1-\varphi)K_s}\left(\frac{d^s p_t}{dt} - \frac{d^f p_f}{dt}\right) + \frac{\kappa_s}{X_{\text{seq}}}\frac{d^s X_s}{dt} + \frac{p_e}{(1-\varphi)\eta_s}. \tag{31}$$

By introducing Darcy's flux instead of fluid velocity in the total mass balance Equation 24 and making use of derived compaction equations together with equations of state Equations 29 and 31, we obtain

$$\nabla_j q_D^j = \frac{\alpha}{K_d}\left(\frac{d^s p_t}{dt} - \frac{1}{B}\frac{d^f p_f}{dt}\right) - \frac{\kappa_r}{X_{\text{seq}}}\frac{d^s X_s}{dt} + \frac{\alpha^v}{\eta_d} p_e \tag{32}$$

Here, B is the analog of Skemton's coefficient, and α is the Biot-Willis parameter. There is the following relation between the three elastic moduli:

$$\frac{1-\varphi}{K_d} = \frac{1}{K_\varphi} + \frac{1}{K_s}, \alpha = 1 - \frac{K_d}{K_s}, B = \frac{\frac{1}{K_d} - \frac{1}{K_s}}{\frac{1}{K_d} - \frac{1}{K_s} + \frac{\varphi}{K_f}} \tag{33}$$

The new coefficients related to the reactive terms are

$$\kappa_s = \frac{X_{\text{seq}}}{1 - X_s} - \frac{\kappa_\varphi}{1-\varphi} - \kappa_d \tag{34}$$

$$\kappa_r = \varphi\kappa_d - \kappa_\varphi + (1-\varphi)\frac{X_{\text{seq}}}{1 - X_s}\frac{\rho_s}{\rho_f} \tag{35}$$

Using an elastic analogy, we introduce the following notations for viscous parameters:

$$\frac{1}{\eta_s} = \frac{1-\varphi}{\eta_d} - \frac{1}{\eta_\varphi}, \alpha^v = \varphi + \frac{\eta_d}{\eta_\varphi} = 1 - \frac{\eta_d}{\eta_s} \tag{36}$$

If using effective moduli obtained in Section 2 in Equations 33 and 36, we obtain simplified expressions for the Biot-Willis parameter, namely:

$$\alpha = \alpha^v = 1/\Theta \tag{37}$$

In the non-reacting limit, $X_s = \text{const}$, Equation 31 and reduces to poroviscoelastic equations of Yarushina and Podladchikov (2015). In general, in reactive materials, the compressibility and viscosity of solid grains, K_s and η_s,

can change as one mineral converts to another. They can even become negative, for example, during devolatilization reactions, when stress enhances the reaction and thus reduces density. And only in the non-reacting limit, K_s and η_s become constant and satisfy all the usual limits, including elastic Gassmann's relation.

4. Effect of Swelling/Shrinkage on Fluid Flow

In this section, we will explore how the interplay between reaction and deformation affects the fluid flow and each other. We consider a simple hydration reaction associated with solid volume increase. This can be serpentinization at mid-ocean ridges, associated with a change in solid volume of ∼50% in a closed system. Or this can be the hydration of metal oxides added to cement as expanding agents. It can also be the hydration of smectites in the reservoirs affecting the permeability of the caprock. We consider a single reaction and assume that solid mass is conserved, that is, reactive fluid does not bring additional solids.

4.1. Nondimensional 1D Governing Equations

The non-dimensional equations are obtained by choosing the model scale, L, as the length scale, the solid bulk modulus as the pressure scale $P = K_0 = G_1/\varphi_0$; characteristic time for reaction as the time scale $T = \tau$. We ignore the influence of shear stresses and gravity forces for simplicity by assuming $\nabla_j \tau_{ij} = 0$. In 1D, this is equivalent to the assumption that $p_t = \text{const}$. In the following, we introduce two nondimensional numbers: the Dahmköhler number comparing the chemical reaction timescale to the transport phenomena ($\text{Da} = \frac{\tau}{T_D} = \frac{k_0 K_0 \tau}{\mu_f L^2}$) and the Deborah number comparing the characteristic times for viscoelastic relaxation to the reaction timescale ($\text{De} = \frac{\eta_0}{TP} = \frac{\mu_1}{\tau G_1}$). Then, the system of governing equations becomes

$$\frac{\partial v_x'}{\partial x'} = -\frac{1}{K_d'}\left(\frac{dp_t'}{dt'} - \frac{dp_f'}{dt'}\right) + \kappa_d \frac{d\xi}{dt'} - \frac{1}{De}\frac{p_t' - p_f'}{\eta_d'} \tag{38}$$

$$\frac{\partial q_D^{x\prime}}{\partial x'} = \frac{\alpha}{K_d'}\left(\frac{dp_t'}{dt'} - \frac{1}{B}\frac{dp_f'}{dt'}\right) - \kappa_r \frac{d\xi}{dt'} + \frac{\alpha_v}{De}\frac{p_e'}{\eta_d'} \tag{39}$$

$$q_D^{x\prime} = -\text{Da}\left(\frac{\varphi}{\varphi_0}\right)^n \frac{\partial p_f'}{\partial x'} \tag{40}$$

$$\frac{d\xi}{dt'} = \left(\frac{\varphi}{\varphi_p}\right)^{2/3}(1-\xi) \tag{41}$$

$$\frac{K_f'}{\rho_f'}\frac{d\rho_f'}{dt'} = \frac{dp_f'}{dt'} \tag{42}$$

$$\frac{1}{\rho_s'}\frac{d\rho_s'}{dt'} = \frac{1}{(1-\varphi)K_s'}\left(\frac{dp_t'}{dt'} - \frac{dp_f'}{dt'}\right) + \kappa_s \frac{d\xi}{dt'} + \frac{1}{\text{De}}\frac{p_e'}{1-\varphi} \tag{43}$$

$$\frac{d\varphi}{dt'} = -\frac{1}{K_\varphi'}\frac{dp_e'}{dt'} - \kappa_\varphi \frac{d\xi}{dt'} - \frac{1}{\text{De}}\frac{p_e'}{\eta_\varphi'} \tag{44}$$

where $\frac{1}{K_d'} = \frac{K_0}{K_d}, \frac{1}{K_f'} = \frac{K_0}{K_f}, \frac{1}{K_\varphi'} = \frac{K_0}{K_\varphi}, \frac{1}{K_s'} = \frac{K_0}{K_s}, \frac{1}{\eta_d'} = \frac{\eta_0}{\eta_d}, \frac{1}{\eta_\varphi'} = \frac{\eta_0}{\eta_\varphi}$. Equations 38–44 form a closed system of equations for p_f, φ, ξ, ρ_s, ρ_f, q_D^x, v_x. The power-law dependence of permeability on porosity Equation 30 is assumed here.

4.2. Serpentinization and Mineral Expansion

Malvoisin et al. (2021) showed that including reactive terms in either the porosity or volume change equation leads to different results. We will now estimate how reactive terms in both compaction equations influence the outcome and when classical pore clogging or complete reaction might be expected. Following Malvoisin et al. (2021), we consider a one-dimensional domain of length L undergoing serpentinization at 200°C, 50 MPa total lithostatic pressure, and 40 MPa initial fluid pressure. During simulation, we impose a constant fluid pressure of 40 MPa

Table 3
Parameters Used in Simulations

Parameter	Symbol	Value
Initial solid/fluid density ratio	ρ_s/ρ_f	3.3
Permeability exponent	n	3
Porosity above which a porous rock has the same reactive surface area as a powder	φ_p	0.38
Elastic moduli change during the reaction	G_2/G_1	0.45
Fluid compressibility	$1/K_f$	$36/K_0$
Solid density changes during the reaction	Θ	0.8
Effective viscosity changes during the reaction	μ_2/μ_1	0.5
Characteristic pressure scale	K_0	80 GPa
Background permeability	k_0	10^{-19}–10^{-17} m^2
Viscosity of water	μ_f	10^{-4} Pa · s
Characteristic time for reaction	τ	10^7–10^8 s
Length of numerical model	L	1–10 m

at the model boundaries. The domain is assumed horizontal so that gravity terms can be neglected. It is initially exclusively composed of olivine (dunite; $\xi = 0$). The initial porosity, $\varphi_0 = 0.01$, allows fluid transport and reaction initiation. The parameters used in the model are summarized in Table 3. The bulk modulus of serpentine, $K_0 = 80$ GPa (Mookherjee & Stixrude, 2009), is adopted as a representative pressure scale. For the alterations in density and elastic moduli during the reaction, we adopt the values for serpentinite ($\rho = 2.6$ g/cm^3, $G = 36$ GPa) as reported by David et al. (2019). Likewise, for olivine, we use the values ($\rho = 3.3$ g/cm^3, $G = 80$ GPa) documented by Abramson et al. (1997). For the minimum porosity for which a porous rock has the same reactive surface area as a powder, a value of $\phi_p = 0.38$ is employed based on the experimental findings of Llana-Fúnez et al. (2007). Permeability, reaction rate, solid shear viscosity, and domain length are not well constrained. Thus, for permeability, we consider a range of $k_0 = 10^{-19}$–10^{-17} m^2, as reported by Farough et al. (2016) and Godard et al. (2013) based on the fluid flow experiments conducted on peridotite. For solid viscosity, we consider a range of values between 10^{17} to 10^{20} Pa s based on data on high-pressure creep of serpentine from Hilairet et al. (2007). Given that there is not much data on the viscosity of olivine at 200°C, we assume roughly the same viscosity change during reaction as for elastic moduli. For the characteristic reaction time and size of the domain, we follow Malvoisin et al. (2021) and consider values between $\tau = 10^7$–10^8 s and $L = 1$–10 m. These parameter estimates determined Da and De values from 1 to 10^5 and 10^{-1} to 10^3, respectively.

We rely on a finite-difference discretization of Equations 38–44 and employ a second-order pseudo-transient relaxation approach to achieve an implicit solution of the nonlinear coupled system of equations (Omlin et al., 2018; Räss et al., 2016, 2019; L. H. Wang et al., 2022). We ensure the convergence of the global residual for the fully nonlinear and coupled system at each time step to guarantee the accuracy of the results. The numerical algorithm is written in MATLAB. We predict the evolution of porosity, pressures, rock hydration degree, and solid volume change for a wide range of Deborah and Dahmköhler numbers.

Pore water gradually reacts with olivine, reducing porosity and fluid pressure (Figure 4). External fluid supply keeps fluid pressure constant at the boundaries, which causes the nonhomogeneous distribution of pressure, porosity, and reaction progress in the 1D domain. The evolution of a reactive water-rock system can follow two different scenarios. First, the ongoing reaction might lead to the precipitation of reactive products and full consumption of the fluid so that fluid pressure in the center of the domain is reduced to zero (Figure 5a). This prevents further reaction due to the absence of necessary fluid even though porosity is still available. The reaction progress is very limited in this case. This prediction aligns with the experimental findings of Godard et al. (2013), who injected seawater into permeable olivine to explore the relationships between hydration reactions and hydro-dynamic properties. They report that despite minimal variation in porosity throughout the experiment, fluid circulation was constrained as the reaction advanced. In the end, when fluid circulation was lost, only 10% of olivine was converted, which is close to the maximum reaction progress achieved in our model presented in Figure 5a. Our model additionally anticipates a slight volume expansion of approximately 3% for the reaction, reaching 8% (right panel in Figure 5a). These values align closely with the experimental findings of Klein and Le Roux (2020), who

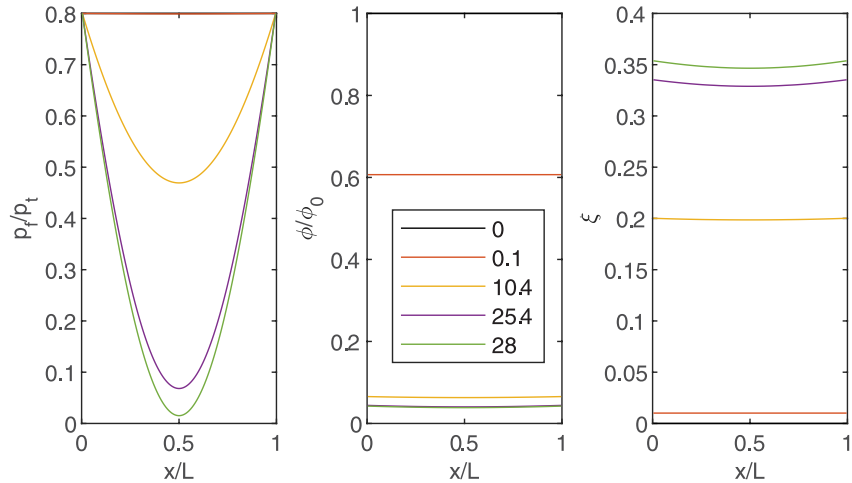

Figure 4. Evolution of normalized fluid pressure, porosity, and reaction progress in a 1D column in time. Colors correspond to different nondimensional times, as indicated in the figure legend.

investigated volume increases during serpentinization. Their study reported a volume increase of up to 2.5% for samples, with reaction progress reaching 6%.

In the second typical scenario observed in our simulations, solid volume expansion takes over after an initial stage of pore-clogging, and the porosity reduction is drastically slowed (Figure 5b). Qualitatively, the solution presented in Figure 5b is very similar to that of Malvoisin et al. (2021). After the initial decrease, fluid pressure returns to its initial levels, which helps to maintain further reaction and eventually complete the reaction. For the case in Figure 5b, the volume expansion exceeds 40%. And indeed, observations show that serpentinization generally results in volume expansion between 25% and 53% (Germanovich et al., 2012). Klein and Le Roux (2020) report a 44% volume increase in serpentinized domains based on their laboratory experiments. The degree of expansion largely depends on the reaction progress, ratio of densities, and ratio of elastic (viscous) moduli.

Observations show that the degree of serpentinization in natural samples might vary from <10% to >90% (Beard et al., 2009; Oufi et al., 2002). Whether the reaction will be completed in viscoelastic materials depends on the nondimensional Dahmköhler and Deborah numbers (Figure 6). To complete the reaction, large Dahmköhler and Deborah numbers are required (Figure 6a). At the end of the reaction, porosity will be reduced by almost two orders of magnitude compared to the initial value. Completion of the reaction hinges on the relative importance of the volume expansion and pore-clogging terms given by the ratio of effective reactive compressibilities in Equation 23. This ratio itself depends on the constitutive stress-strain relations for the rock matrix. Our results show that dissolution-precipitation models can be used at very small Da < 10. Microstructural observations reveal that advancing reaction might be accompanied by reaction-induced cracking around the pores and grain boundaries when locally generated stresses are high enough (e.g., Lesti et al., 2013; Malvoisin et al., 2017). In such cases, the viscoelastic model might not be the best choice, and pore-scale failure processes will need to be considered. We leave this further development to future publications.

Note that in all our simulations, we assumed total pressure was constant. This approximation corresponds to an idealized system in which reaction-induced change in volume is fully accommodated by deformation and is valid in, for example, the vertical direction where the overburden would be held fixed. It provides maximum estimates for reaction-induced deformation. Another end-member assumption is that of no lateral strain, which might be applicable in a horizontal direction. It provides maximum estimates for total pressure variations during the reaction. Malvoisin et al. (2021) considered both cases and found that assuming a constant solid volume leads to zero serpentinization rate, and the reaction cannot be completed. Thus, the evolutions of the extent of reaction and porosity are similar to the classical dissolution-precipitation models in case of no lateral strain.

5. Conclusions

It is often assumed that reaction processes are transport-dominated, that is, all dissolved material is carried away by pore fluid and then precipitates on the available pore space, leading to clogging and reduced permeability.

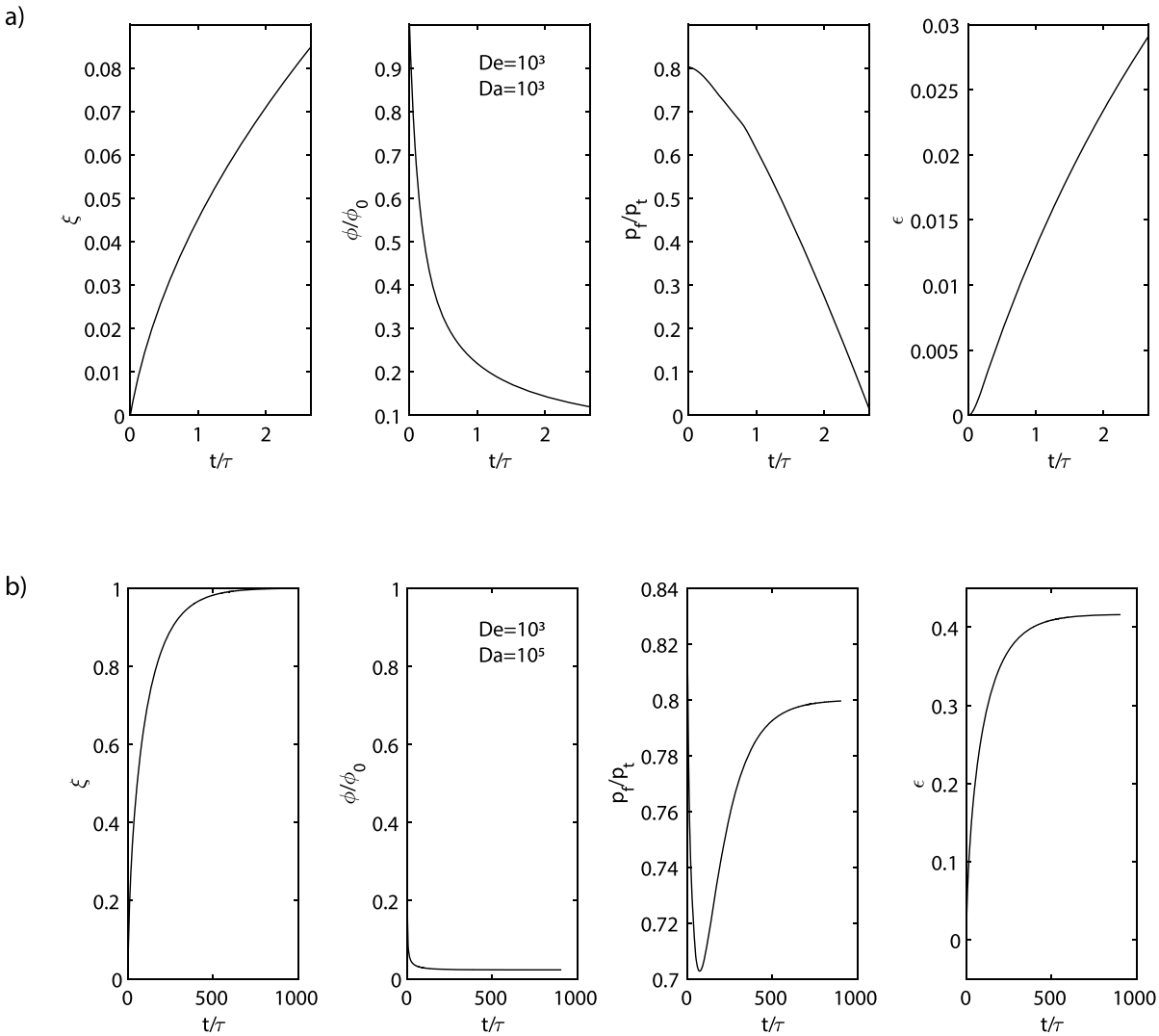

Figure 5. Typical evolution of normalized reaction progress, porosity, fluid pressure, and volumetric deformation with time for two different values of Dahmköhler number showing incomplete reaction for Da = 10^3 (a) and complete reaction for Da = 10^5 (b). Time evolution plots represent the midpoint of the 1D domain at $x = L/2$.

Based on recent observations (Malvoisin et al., 2021; Putnis et al., 2021), we developed a micromechanical model where volume change produced by the reaction is accommodated by matrix deformation rather than clogging of pore space. This allows the preservation of the pore space to sustain the further reaction. The new constitutive equations for porosity evolution and bulk volume changes are formulated. While in the classical dissolution/precipitation models, the reactive term enters only the porosity equation, the new model also predicts reaction-produced volume expansion. The relative importance of porosity clogging versus volume expansion depends on the porosity and reaction progress. We show that dissolution/precipitation models can be accurate for small Dahmköhler numbers or at initial reaction stages. In low porosity materials or as porosity gets clogged due to reaction, volume expansion becomes more important than porosity clogging, allowing further accommodation of reaction. In the non-reactive limit, the new constitutive equations reduce to our previous viscoelastic model (Yarushina & Podladchikov, 2015). The model gives closed-form expressions for the dependence of elastic moduli and creep rates on solid grains' reaction progress, porosity, and material parameters.

The effect of new constitutive equations on fluid flow was studied numerically on a simple example of mineral hydration associated with solid volume increase, such as during serpentinization, cement hydration, or hydration of quicklime or periclase that were suggested as volume-expanding additives to cement compositions. We show that achieving 100% of the reaction strongly depends on the form of the porosity equation and equation for

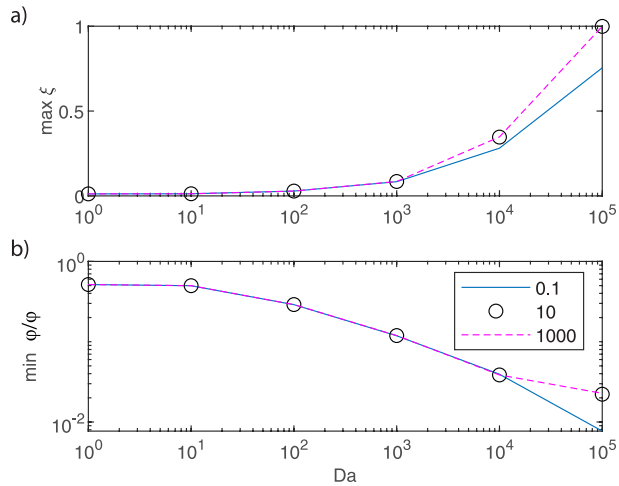

Figure 6. Summary of the simulation results showing maximum reaction progress reached (a) and corresponding remaining porosity (b) for various Da numbers. Different line styles correspond to different De numbers, as indicated in the figure legend.

bulk deformation. The viscoelastic model allows complete reaction at large Deborah and Dahmköhler numbers, although a significant porosity reduction accompanies the reaction progress. We show that the degree of volume expansion largely depends on the ability to complete the reaction.

Data Availability Statement

The numerical code used in this study is published on Zenodo, https://doi.org/10.5281/zenodo.8280019 (L. H. Wang et al., 2023).

Acknowledgments
This paper was partially carried out within SWIPA, Center for Subsurface Well Integrity, Plugging and Abandonment, with financial support from the Research Council of Norway (RCN project no. 309646), AkerBP ASA, Equinor Energy AS, and Wintershall DEA Norway AS. We thank Eric Dunham and an anonymous reviewer for their helpful comments.

References

Abramson, E. H., Brown, J. M., Slutsky, L. J., & Zaug, J. M. (1997). The elastic constants of San Carlos olivine to 17 GPa. *Journal of Geophysical Research*, *102*(B6), 12253–12263. https://doi.org/10.1029/97jb00682

Aharonov, E., Tenthorey, E., & Scholz, C. H. (1998). Precipitation sealing and diagenesis - 2. Theoretical analysis. *Journal of Geophysical Research*, *103*(B10), 23969–23981. https://doi.org/10.1029/98jb02230

Beard, J. S., Frost, B. R., Fryer, P., McCaig, A., Searle, R., Ildefonse, B., et al. (2009). Onset and progression of serpentinization and magnetite formation in Olivine-rich Troctolite from IODP Hole U1309D. *Journal of Petrology*, *50*(3), 387–403. https://doi.org/10.1093/petrology/egp004

Biot, M. A. (1941). General theory of three-dimensional consolidation. *Journal of Applied Physics*, *12*(2), 155–164. https://doi.org/10.1063/1.1712886

Boait, F. C., White, N. J., Bickle, M. J., Chadwick, R. A., Neufeld, J. A., & Huppert, H. E. (2012). Spatial and temporal evolution of injected CO_2 at the Sleipner Field, North Sea. *Journal of Geophysical Research*, *117*(B3), B03309. https://doi.org/10.1029/2011jb008603

Busch, A., Bertier, P., Gensterblum, Y., Rother, G., Spiers, C. J., Zhang, M., & Wentinck, H. M. (2016). On sorption and swelling of CO_2 in clays. *Geomechanics and Geophysics for Geo-energy and Geo-resources*, *2*(2), 111–130. https://doi.org/10.1007/s40948-016-0024-4

Clark, D. E., Oelkers, E. H., Gunnarsson, I., Sigfusson, B., Snaebjornsdottir, S. O., Aradottir, E. S., & Gislason, S. R. (2020). CarbFix2: CO_2 and H_2S mineralization during 3.5 years of continuous injection into basaltic rocks at more than 250 degrees C. *Geochimica et Cosmochimica Acta*, *279*, 45–66. https://doi.org/10.1016/j.gca.2020.03.039

David, E. C., Brantut, N., Hansen, L. N., & Jackson, I. (2019). Low-frequency measurements of seismic moduli and attenuation in antigorite serpentinite. *Geophysical Research Letters*, *46*(4), 1993–2002. https://doi.org/10.1029/2018gl081271

Elenius, M., Skurtveit, E., Yarushina, V., Baig, I., Sundal, A., Wangen, M., et al. (2018). Assessment of CO_2 storage capacity based on sparse data: Skade Formation. *International Journal of Greenhouse Gas Control*, *79*, 252–271. https://doi.org/10.1016/j.ijggc.2018.09.004

Evans, O., Spiegelman, M., & Kelemen, P. B. (2018). A poroelastic model of serpentinization: Exploring the interplay between rheology, surface energy, reaction, and fluid flow. *Journal of Geophysical Research: Solid Earth*, *123*(10), 8653–8675. https://doi.org/10.1029/2017jb015214

Fabbri, A., Corvisier, J., Schubnel, A., Brunet, F., Goffe, B., Rimmele, G., & Barlet-Gouedard, V. (2009). Effect of carbonation on the hydro-mechanical properties of Portland cements. *Cement and Concrete Research*, *39*(12), 1156–1163. https://doi.org/10.1016/j.cemconres.2009.07.028

Farough, A., Moore, D. E., Lockner, D. A., & Lowell, R. P. (2016). Evolution of fracture permeability of ultramafic rocks undergoing serpentinization at hydrothermal conditions: An experimental study. *Geochemistry, Geophysics, Geosystems*, *17*(1), 44–55. https://doi.org/10.1002/2015gc005973

Fletcher, R. C., & Merino, E. (2001). Mineral growth in rocks: Kinetic-rheological models of replacement, vein formation, and syntectonic crystallization. *Geochimica et Cosmochimica Acta*, *65*(21), 3733–3748. https://doi.org/10.1016/S0016-7037(01)00726-8

Gassmann, F. (1951). Über die elastizität poröser medien. *Vierteljahrsschrift der Naturforschenden Gesellschaft in Zürich*, *96*, 1–23.

Germanovich, L. N., Genc, G., Lowell, R. P., & Rona, P. A. (2012). Deformation and surface uplift associated with serpentinization at mid-ocean ridges and subduction zones. *Journal of Geophysical Research*, *117*(B7), B07103. https://doi.org/10.1029/2012jb009372

Godard, M., Luquot, L., Andreani, M., & Gouze, P. (2013). Incipient hydration of mantle lithosphere at ridges: A reactive-percolation experiment. *Earth and Planetary Science Letters*, *371*, 92–102. https://doi.org/10.1016/j.epsl.2013.03.052

Heap, M. J., Baud, P., Meredith, P. G., Vinciguerra, S., Bell, A. F., & Main, I. G. (2011). Brittle creep in basalt and its application to time-dependent volcano deformation. *Earth and Planetary Science Letters*, *307*(1–2), 71–82. https://doi.org/10.1016/j.epsl.2011.04.035

Hilairet, N., Reynard, B., Wang, Y. B., Daniel, I., Merkel, S., Nishiyama, N., & Petitgirard, S. (2007). High-pressure creep of serpentine, interseismic deformation, and initiation of subduction. *Science*, *318*(5858), 1910–1913. https://doi.org/10.1126/science.1148494

Hu, Y. Q., Watanabe, M., Aida, C., & Horio, M. (2006). Capture of H_2S by limestone under calcination conditions in a high-pressure fluidized-bed reactor. *Chemical Engineering Science*, *61*(6), 1854–1863. https://doi.org/10.1016/j.ces.2005.10.006

Idiart, A. E., Lopez, C. M., & Carol, I. (2011). Chemo-mechanical analysis of concrete cracking and degradation due to external sulfate attack: A meso-scale model. *Cement and Concrete Composites*, *33*(3), 411–423. https://doi.org/10.1016/j.cemconcomp.2010.12.001

Kelemen, P. B., & Hirth, G. (2012). Reaction-driven cracking during retrograde metamorphism: Olivine hydration and carbonation. *Earth and Planetary Science Letters*, *345*, 81–89. https://doi.org/10.1016/j.epsl.2012.06.018

Kelemen, P. B., & Matter, J. (2008). In situ carbonation of peridotite for CO_2 storage. *Proceedings of the National Academy of Sciences of the United States of America*, *105*(45), 17295–17300. https://doi.org/10.1073/pnas.0805794105

Kieffer, B., Jové, C. F., Oelkers, E. H., & Schott, J. (1999). An experimental study of the reactive surface area of the Fontainebleau sandstone as a function of porosity, permeability, and fluid flow rate. *Geochimica et Cosmochimica Acta*, *63*(21), 3525–3534. https://doi.org/10.1016/S0016-7037(99)00191-X

Klein, F., & Le Roux, V. (2020). Quantifying the volume increase and chemical exchange during serpentinization. *Geology*, *48*(6), 552–556. https://doi.org/10.1130/G47289.1

Kutchko, B. G., Strazisar, B. R., Hawthorne, S. B., Lopano, C. L., Miller, D. J., Hakala, J. A., & Guthrie, G. D. (2011). H_2S-CO_2 reaction with hydrated Class H well cement: Acid-gas injection and CO_2 Co-sequestration. *International Journal of Greenhouse Gas Control*, *5*(4), 880–888. https://doi.org/10.1016/j.ijggc.2011.02.008

Lesti, M., Tiemeyer, C., & Plank, J. (2013). CO_2 stability of Portland cement based well cementing systems for use on carbon capture & storage (CCS) wells. *Cement and Concrete Research*, *45*, 45–54. https://doi.org/10.1016/j.cemconres.2012.12.001

Lichtner, P. C. (1988). The quasi-stationary state approximation to coupled mass-transport and fluid-rock interaction in a porous-medium. *Geochimica et Cosmochimica Acta*, *52*(1), 143–165. https://doi.org/10.1016/0016-7037(88)90063-4

Llana-Fúnez, S., Brodie, K. H., Rutter, E. H., & Arkwright, J. C. (2007). Experimental dehydration kinetics of serpentinite using pore volumometry. *Journal of Metamorphic Geology*, *25*(4), 423–438. https://doi.org/10.1111/j.1525-1314.2007.00703.x

Malvoisin, B., Brantut, N., & Kaczmarek, M. A. (2017). Control of serpentinisation rate by reaction-induced cracking. *Earth and Planetary Science Letters*, *476*, 143–152. https://doi.org/10.1016/j.epsl.2017.07.042

Malvoisin, B., Podladchikov, Y. Y., & Myasnikov, A. V. (2021). Achieving complete reaction while the solid volume increases: A numerical model applied to serpentinisation. *Earth and Planetary Science Letters*, *563*, 116859. https://doi.org/10.1016/j.epsl.2021.116859

Malvoisin, B., Zhang, C., Muntener, O., Baumgartner, L. P., Kelemen, P. B., & Party, O. D. P. S. (2020). Measurement of volume change and mass transfer during serpentinization: Insights from the Oman drilling project. *Journal of Geophysical Research: Solid Earth*, *125*(5), e2019JB018877. https://doi.org/10.1029/2019JB018877

Marzal, R. M. E., & Scherer, G. W. (2008). Crystallization of sodium sulfate salts in limestone. *Environmental Geology*, *56*(3–4), 605–621. https://doi.org/10.1007/s00254-008-1441-7

Matter, J. M., Stute, M., Snæbjörnsdottir, S. Ó., Oelkers, E. H., Gislason, S. R., Aradottir, E. S., et al. (2016). Rapid carbon mineralization for permanent disposal of anthropogenic carbon dioxide emissions. *Science*, *352*(6291), 1312–1314. https://doi.org/10.1126/science.aad8132

Merino, E., & Dewers, T. (1998). Implications of replacement for reaction-transport modeling. *Journal of Hydrology*, *209*(1–4), 137–146. https://doi.org/10.1016/S0022-1694(98)00150-4

Minde, M. W., & Hiorth, A. (2020). Compaction and fluid-rock interaction in chalk insight from modelling and data at pore-core-and field-scale. *Geosciences*, *10*(1), 6. https://doi.org/10.3390/geosciences10010006

Mookherjee, M., & Stixrude, L. (2009). Structure and elasticity of serpentine at high-pressure. *Earth and Planetary Science Letters*, *279*(1–2), 11–19. https://doi.org/10.1016/j.epsl.2008.12.018

Neville, A. M., Dilger, W. H., & Brooks, J. J. (1983). *Creep of plain and structural concrete* (p. 361). Construction Press.

Omlin, S., Malvoisin, B., & Podladchikov, Y. Y. (2017). Pore fluid extraction by reactive solitary waves in 3-D. *Geophysical Research Letters*, *44*(18), 9267–9275. https://doi.org/10.1002/2017gl074293

Omlin, S., Räss, L., & Podladchikov, Y. Y. (2018). Simulation of three-dimensional viscoelastic deformation coupled to porous fluid flow. *Tectonophysics*, *746*, 695–701. https://doi.org/10.1016/j.tecto.2017.08.012

Ostapenko, G. T. (1976). Excess pressure upon solid-phases arising during reactions of hydration (according to experimental-data of periclase hydration). *Geokhimiya+*(6), 824–844.

Oufi, O., Cannat, M., & Horen, H. (2002). Magnetic properties of variably serpentinized abyssal peridotites. *Journal of Geophysical Research*, *107*(B5), EPM 3-1–EPM 3-19. https://doi.org/10.1029/2001jb000549

Perchuk, A. L., Zakharov, V. S., Gerya, T. V., & Griffin, W. L. (2023). Flat subduction in the Early Earth: The key role of discrete eclogitization kinetics. *Gondwana Research*, *119*, 186–203. https://doi.org/10.1016/j.gr.2023.03.015

Putnis, C. V., Wang, L., Ruiz-Agudo, E., Ruiz-Agudo, C., & Renard, F. (2021). Crystallization via nonclassical pathways: Nanoscale imaging of mineral surfaces. In X. Zhang (Ed.), *Crystallization via nonclassical pathways* (pp. 1–35). American Chemical Society. https://doi.org/10.1021/bk-2021-1383.ch001

Räss, L., Duretz, T., & Podladchikov, Y. Y. (2019). Resolving hydromechanical coupling in two and three dimensions: Spontaneous channelling of porous fluids owing to decompaction weakening. *Geophysical Journal International*, *218*(3), 1591–1616. https://doi.org/10.1093/gji/ggz239

Räss, L., Yarushina, V., Duretz, T., & Podladchikov, Y. (2016). High-resolution numerical modelling to resolve the dynamics of pipe structures in porous media. In *Paper presented at ECMOR XV - 15th European conference on the mathematics of oil recovery*.

Riis, F., & Halland, E. (2014). CO_2 storage atlas of the Norwegian Continental shelf: Methods used to evaluate capacity and maturity of the CO_2 storage potential. In *12th International conference on greenhouse gas control technologies, GHGT-12* (Vol. 63, pp. 5258–5265). https://doi.org/10.1016/j.egypro.2014.11.557

Rutter, E. H. (1976). Kinetics of rock deformation by pressure solution. *Philosophical Transactions of the Royal Society of London Series A-Mathematical Physical and Engineering Sciences*, *283*(1312), 203–219.

Sabitova, A. I., Yarushina, V. M., Stanchits, S. A., Stukachev, V. I., & Myasnikov, A. V. (2021). Experimental compaction and dilation of porous rocks during triaxial creep and stress relaxation. *Rock Mechanics and Rock Engineering*, *54*(11), 5781–5805. https://doi.org/10.1007/s00603-021-02562-4

Schaef, H. T., Ilton, E. S., Qafoku, O., Martin, P. F., Felmy, A. R., & Rosso, K. M. (2012). In situ XRD study of Ca^{2+} saturated montmorillonite (STX-1) exposed to anhydrous and wet supercritical carbon dioxide. *International Journal of Greenhouse Gas Control*, *6*, 220–229. https://doi.org/10.1016/j.ijggc.2011.11.001

Schmeling, H., Kruse, J. P., & Richard, G. (2012). Effective shear and bulk viscosity of partially molten rock based on elastic moduli theory of a fluid filled poroelastic medium. *Geophysical Journal International*, *190*(3), 1571–1578. https://doi.org/10.1111/j.1365-246X.2012.05596.x

Schmid, D. W., Abart, R., Podladchikov, Y. Y., & Milke, R. (2009). Matrix rheology effects on reaction rim growth II: Coupled diffusion and creep model. *Journal of Metamorphic Geology*, *27*(1), 83–91. https://doi.org/10.1111/j.1525-1314.2008.00805.x

Steiger, M. (2005). Crystal growth in porous materials - I: The crystallization pressure of large crystals. *Journal of Crystal Growth*, *282*(3–4), 455–469. https://doi.org/10.1016/j.jcrysgro.2005.05.007

Vralstad, T., Saasen, A., Fjaer, E., Oia, T., Ytrehus, J. D., & Khalifeh, M. (2019). Plug & abandonment of offshore wells: Ensuring long-term well integrity and cost-efficiency. *Journal of Petroleum Science and Engineering*, *173*, 478–491. https://doi.org/10.1016/j.petrol.2018.10.049

Wang, L. H., Yarushina, V. M., Alkhimenkov, Y., & Podladchikov, Y. (2022). Physics-inspired pseudo-transient method and its application in modelling focused fluid flow with geological complexity. *Geophysical Journal International*, *229*(1), 1–20. https://doi.org/10.1093/gji/ggab426

Wang, L. H., Yarushina, V. M., & Podladchikov, Y. Y. (2023). On the constitutive equations for coupled flow, chemical reaction, and deformation of porous media [Software]. Zenodo. https://doi.org/10.5281/zenodo.8280019

Wang, L. L., Bornert, M., Heripre, E., Yang, D. S., & Chanchole, S. (2014). Irreversible deformation and damage in argillaceous rocks induced by wetting/drying. *Journal of Applied Geophysics*, *107*, 108–118. https://doi.org/10.1016/j.jappgeo.2014.05.015

Weyl, P. K. (1959). Pressure solution and the force of crystallization - A phenomenological theory. *Journal of Geophysical Research*, *64*(11), 2001–2025. https://doi.org/10.1029/jz064i011p02001

Wolterbeek, T. K. T., Hangx, S. J. T., & Spiers, C. J. (2016). Effect of CO_2-induced reactions on the mechanical behaviour of fractured wellbore cement. *Geomechanics for Energy and the Environment*, *7*, 26–46. https://doi.org/10.1016/j.gete.2016.02.002

Wolterbeek, T. K. T., van Noort, R., & Spiers, C. J. (2018). Reaction-driven casing expansion: Potential for wellbore leakage mitigation. *Acta Geotechnica*, *13*(2), 341–366. https://doi.org/10.1007/s11440-017-0533-5

Xing, T. G., Ghaffari, H. O., Mok, U., & Pec, M. (2022). Creep of CarbFix basalt: Influence of rock-fluid interaction. *Solid Earth*, *13*(1), 137–160. https://doi.org/10.5194/se-13-137-2022

Yarushina, V. M., & Bercovici, D. (2013). Mineral carbon sequestration and induced seismicity. *Geophysical Research Letters*, *40*(5), 814–818. https://doi.org/10.1002/Grl.50196

Yarushina, V. M., Bercovici, D., & Oristaglio, M. L. (2013). Rock deformation models and fluid leak-off in hydraulic fracturing. *Geophysical Journal International*, *194*(3), 1514–1526. https://doi.org/10.1093/Gji/Ggt199

Yarushina, V. M., Makhnenko, R. Y., Podladchikov, Y. Y., Wang, L. H., & Rass, L. (2021). Viscous behavior of clay-rich rocks and its role in focused fluid flow. *Geochemistry, Geophysics, Geosystems*, *22*(10), e2021GC009949. https://doi.org/10.1029/2021gc009949

Yarushina, V. M., & Podladchikov, Y. Y. (2015). (De)compaction of porous viscoelastoplastic media: Model formulation. *Journal of Geophysical Research: Solid Earth*, *120*(6), 4146–4170. https://doi.org/10.1002/2014JB011258

Zhang, M., & Bachu, S. (2011). Review of integrity of existing wells in relation to CO_2 geological storage: What do we know? *International Journal of Greenhouse Gas Control*, *5*(4), 826–840. https://doi.org/10.1016/j.ijggc.2010.11.006

Zimmerman, R. W. (1991). *Compressibility of sandstones* (p. 173). Elsevier.

Zimmerman, R. W., Somerton, W. H., & King, M. S. (1986). Compressibility of porous rocks. *Journal of Geophysical Research*, *91*(B12), 2765–2777. https://doi.org/10.1029/jb091ib12p12765